

Electric-field-dependent absorption of ZnSe-based quantum wells: The transition from two-dimensional to three-dimensional behavior

D. Merbach and E. Schöll

Institut für Theoretische Physik, Technische Universität Berlin, Hardenbergstraße 36, D-10623 Berlin, Germany

W. Ebeling, P. Michler, and J. Gutowski

Institut für Festkörperphysik, Universität Bremen, P.O. Box 330440, D-28334 Bremen, Germany

(Received 9 April 1998)

The absorption coefficient of $\text{Zn}_x\text{Cd}_{1-x}\text{Se}/\text{ZnS}_y\text{Se}_{1-y}$ quantum-well structures in a strong electric field is investigated as it depends on the quantum-well width. A quantum-mechanical model is developed which fully takes account of the Coulomb interaction leading to intersubband coupling and strong excitonic effects. Numerical results are presented and compared with measurements. The study focuses on the transition regime between the quantum-confined Stark effect, which is found for well widths smaller than the exciton Bohr diameter, and the Franz-Keldysh effect, which corresponds to the limit of wide wells. Our theory allows for a unified treatment of a wide range of quantum-well widths and applied fields, and provides detailed insight into the origin of the structure of the absorption spectrum through a spatially resolved microscopic absorption coefficient. [S0163-1829(98)01840-2]

I. INTRODUCTION

Starting with the first demonstration of blue-green laser diodes,¹ many recent investigations related to ZnSe-based optoelectronics have focused on the development and improvement of laser diodes. In addition, passive devices like electro-optical modulators² and bistable switches are needed. Those devices can be based on the change of the absorption coefficient as a function of an applied voltage.³ For bulk material, this is due to the Franz-Keldysh effect⁴⁻⁶ (FKE). In the case of quasi-two-dimensional semiconductor structures, i.e., quantum wells, the corresponding phenomenon is the quantum-confined Stark effect⁷ (QCSE). Although both effects have been extensively studied in GaAs-based structures (see, e.g., Ref. 8), much less work has been done using ZnSe-based alloys.^{9,10}

Models developed for the theoretical description of such electro-optical modulators essentially focus upon the field-dependent absorption coefficient according to the FKE or the QCSE, respectively. Since the width of the quantum well can be continuously increased from a narrow two-dimensional layer of a few nm to a bulklike layer of the order of 100 nm or more, the QCSE is expected to turn into the FKE with increasing well width. An understanding of this transition is essential for a theoretical description and practical design of heterostructure devices with layers whose thickness is in the intermediate regime.

This transition has previously been investigated in the GaAs-based material system by completely neglecting the Coulomb interaction.¹¹ The authors coined the term “quantum confined Franz-Keldysh effect” (QCFKE) for the electric-field dependence of the absorption coefficient of narrow quantum wells. Subsequently, they showed that the QCFKE turns into the conventional FKE if the quantum well width is increased.¹¹

The neglect of the Coulomb interaction for the discussion of the transition is an acceptable simplification for materials

like GaAs. For ZnSe-based structures, which are characterized by strong excitonic features, the transition from two-dimensional to bulk material is of a very different nature. Thus the concept of the QCFKE is not appropriate for a description of the intermediate regime.

In the zero-field case, the excitonic absorption in bulk materials can be described using the Elliott formula,¹² which has also been adopted to the two-dimensional Coulomb problem.¹³ The excitonic absorption peak is strongly enhanced in the case of two-dimensional structures and the exciton binding energy amounts to four times the bulk value. For the intermediate regime, approaches based on noninteger spatial dimensionality^{14,15} as well as noninteger quantum numbers¹⁶ which interpolate between both limits have been proposed. However, for the purpose of describing electro-optical modulators, these concepts cannot be applied since they do not include the influence of the electric field.

The objective of this paper is to develop a theoretical approach for the field-dependent excitonic absorption coefficient in ZnSe-based structures, and compare it with experimental results. In the center of interest is the investigation of the transition from two-dimensional to bulk behavior. In particular, the theoretical approach is aimed at covering the full transition regime of quantum-well widths, and coping with very high electric fields as appear in the center of *p-i-n* junctions. By comparing this model with simpler approaches which neglect the Coulomb interaction, using material parameters for ZnCdSe/ZnSse structures, the need for the full model will be demonstrated.

The organization of the paper is as follows. In Sec. II, the theoretical model is derived. In Sec. III, the results of numerical simulations are presented, and the transition from two-dimensional to bulk behavior, parametrized by the well width and the electric-field strength, is discussed. In Sec. IV, the simulations are compared with measurements. Finally, some conclusions are drawn in Sec. V.

II. THEORY

The first approach to the theoretical treatment of the quantum-confined Stark effect in III-V semiconductors was limited to the calculation of the spectral shift of the excitonic peak,^{7,17} which was found to be quadratic in the field strength. It was based upon a solution of the one-dimensional Schrödinger equation (in the growth direction) and a variational solution of the exciton problem in the plane of the quantum well. The electric-field-dependent absorption spectrum in the regime of the QCSE may then be modeled by a Gaussian line-shape function centered at the calculated peak energy. The related oscillator strength depends upon the overlap of the corresponding electron and hole wave functions, and upon the exciton wave function.

In the case of more than one discrete level in the conduction- and valence-band quantum well, this procedure is applied to all pairs of levels. Such an approach has been successfully used for the modeling of self-electro-optic-effect devices (SEEDs) based on GaAs/Al_xGa_{1-x}As multiple-quantum well structures.¹⁸ However, this decomposition of the total absorption coefficient into distinct contributions of pairs of levels, each correlated with an exciton, requires that the Coulomb interaction is only a small perturbation of the confinement potential forming the quantum well. This condition is well satisfied in the case of GaAs/Al_xGa_{1-x}As heterostructures but is violated for ZnSe-based structures, due to the much stronger Coulomb interaction and larger exciton binding energy. Typical exciton binding energies are of the order of 6–9 meV in GaAs/Al_xGa_{1-x}As and 30–40 meV in Zn_yCd_{1-y}Se/ZnS_xSe_{1-x} quantum wells, respectively.

As a result, the coupling of the different discrete levels as well as their coupling with bulk continuum states above the quantum well barrier by means of the Coulomb interaction turns out to be essential. The theoretical approach which we develop below takes this coupling into account. As an appropriate formalism we have adopted the density-matrix theory in a real-space representation.¹⁹ This approach has been used, e.g., for a description of nonlinear optical response,²⁰ in particular for the nonresonant optical Stark effect.²¹ For a description of field-dependent absorption in the low-density limit, the real-space concept is preferable to the Fourier-space formalism because spatially dependent quantities naturally arise. This approach readily provides the possibility to discuss the transition from two- to three-dimensional behavior of the absorption coefficient if the quantum-well width is increased.

First, the equation for the microscopic polarization induced by the exciting electromagnetic wave will be set up. In order to solve this equation, we perform a series expansion of the polarization on the basis of the eigenfunctions of the one-dimensional Schrödinger equation for the quantum-well potential. The fast convergence of the expansion allows for an appropriate truncation which is necessary for the numerical solution. Finally, the absorption coefficient is related to the imaginary part of the polarization.

In the second quantized form the two-band Hamiltonian of the system is given by

$$\hat{\mathcal{H}} = \hat{\mathcal{H}}_A + \hat{\mathcal{H}}_{EM} + \hat{\mathcal{H}}_M \quad (1)$$

where

$$\hat{\mathcal{H}}_A = \frac{1}{2} \hbar \omega_g \sum_j (\hat{c}_j^\dagger \hat{c}_j - \hat{d}_j \hat{d}_j^\dagger) \quad (2)$$

is the free Hamiltonian, $E_g = \hbar \omega_g$ is the band gap,

$$\hat{\mathcal{H}}_{EM} = - \sum_j M_0 (\hat{d}_j \hat{c}_j + \hat{c}_j^\dagger \hat{d}_j^\dagger) E_j \quad (3)$$

contains the interaction with an electromagnetic wave E_j within the dipole approximation (dipole matrix element M_0), and

$$\hat{\mathcal{H}}_M = \sum_{i,k} T_{ik}^c \hat{c}_i^\dagger \hat{c}_k + T_{ik}^v \hat{d}_i^\dagger \hat{d}_k \quad (4)$$

describes the coupling in tight-binding approximation (matrix elements T_{ik}^c and T_{ik}^v). Here \hat{c}_j^\dagger (\hat{c}_j) and \hat{d}_j^\dagger (\hat{d}_j) denote the creation (annihilation) operators for an electron and a hole, respectively, at site j .

Using Heisenberg's equations of motion a set of equations for the expectation values of the bilocal operators $\hat{Y}_{ij} = \hat{d}_i \hat{c}_j$, $\hat{C}_{ij} = \hat{c}_i^\dagger \hat{c}_j$, and $\hat{D}_{ij} = \hat{d}_i^\dagger \hat{d}_j$ can be derived. Bilocal dynamic variables are needed, since electrons and holes can move independently. Changing the position indices i and j to continuous coordinates r_1 and r_2 , and normalizing all quantities by the volume element Ω , we can transform to continuous densities and polarizations, e.g., the interband operator

$$\hat{Y}_{ij} \rightarrow \hat{Y}(\mathbf{r}_1, \mathbf{r}_2) / \Omega \equiv \hat{Y}^{cv}, \quad (5)$$

where the superscripts c and v denote the conduction and valence bands, respectively. The expectation values of the diagonal elements of \hat{C} , \hat{D} , and \hat{Y} are related to the usual densities of electrons and holes, and the polarization, respectively. Since we are interested in the absorption spectrum in the low-excitation limit, the densities will be neglected in the following.

To apply the two-band model to ZnSe-based quantum-well structures, some refinements are necessary. The most important extension of the model is the inclusion of the Coulomb interaction. Further, the quantum-well potential and the applied static electric field F are added. It is convenient to introduce the relative coordinate $\mathbf{r} = \mathbf{r}_2 - \mathbf{r}_1 \equiv \mathbf{r}_e - \mathbf{r}_h$ and the center-of-mass coordinate $\mathbf{R} = (m_e \mathbf{r}_e + m_h \mathbf{r}_h) / (m_e + m_h)$. The geometry of the quantum-well structure can be best described by cylindrical coordinates $\mathbf{r} = (\rho, z)$. The projections of the relative coordinate \mathbf{r} and the electron and hole coordinates \mathbf{r}_e and \mathbf{r}_h onto the quantum-well plane are denoted by ρ , ρ_e , and ρ_h , respectively. The respective normal coordinates are z , z_e , and z_h . Z is the projection of the center-of-mass coordinate \mathbf{R} onto the normal. For a monochromatic electromagnetic wave of frequency ω and complex amplitude E_ω , the basic equation for the coherent electron-hole interband amplitude $Y^{vc} = \langle \hat{Y}^{vc} \rangle$ is given by¹⁹

$$[-\hbar(\omega + i\Gamma) + \hbar\Omega_{eh}(\mathbf{r}_e, \mathbf{r}_h)] Y^{vc}(\mathbf{r}_e, \mathbf{r}_h, \omega) = M^{vc}(\mathbf{r}) E_\omega(\mathbf{R}) \quad (6)$$

with

$$\Omega_{eh} = \omega_g + \Omega^{\perp,e} + \Omega^{\perp,h} + \Omega^{\parallel,e} + \Omega^{\parallel,h} + \Omega^{\text{Coul}}, \quad (7a)$$

$$\hbar\Omega^{\perp,e} = -\frac{\hbar^2}{2m_e} \nabla_{z_e}^2 + E_C(z_e) - eFz_e, \quad (7b)$$

$$\hbar\Omega^{\perp,h} = -\frac{\hbar^2}{2m_{h,\perp}} \nabla_{z_h}^2 + E_V(z_h) + eFz_h, \quad (7c)$$

$$\hbar\Omega^{\parallel,e} = -\frac{\hbar^2}{2m_e} \nabla_{\rho_e}^2, \quad (7d)$$

$$\hbar\Omega^{\parallel,h} = -\frac{\hbar^2}{2m_{h,\parallel}} \nabla_{\rho_h}^2, \quad (7e)$$

$$\hbar\Omega^{\text{Coul}} = -\frac{e^2}{4\pi\epsilon_0\epsilon} \frac{1}{\sqrt{(z_e - z_h)^2 + (\rho_e - \rho_h)^2}}. \quad (7f)$$

Here Γ is a phenomenological linewidth accounting for dephasing, mainly due to exciton-phonon interaction at room temperature, but also influenced by alloy fluctuations, interface roughness etc., and $M^{vc}(\mathbf{r})$ is the interband dipole density. The electric field F is applied perpendicular to the quantum-well plane, and $E_C(z_e)$ and $E_V(z_h)$ describe the modulation of the conduction- and valence-band edges due to the confining potential. The effective electron and hole masses for in-plane and perpendicular motions are denoted by $m_{e/h,\parallel}$ and $m_{e/h,\perp}$, respectively, and ϵ_0 and ϵ are the absolute and relative permittivities.

The chosen procedure for the solution of Eq. (6) is to expand the interband amplitude Y^{vc} into solutions of the one-dimensional perpendicular Schrödinger equations for the electron and hole, which are given by

$$\hbar\Omega^{\perp,e} \psi_n^e(z_e) = E_n^e \psi_n^e(z_e), \quad (8a)$$

$$\hbar\Omega^{\perp,h} \psi_m^h(z_h) = E_m^h \psi_m^h(z_h). \quad (8b)$$

The one-dimensional wave functions $\psi^e(z_e)$ and $\psi^h(z_h)$ are used as basis for the expansion according to

$$Y^{vc}(\mathbf{r}_e, \mathbf{r}_h, \omega) = E_\omega \sum_{m,n} Y_{m,n}^{vc}(\rho, \omega) \psi_n^e(z_e) \psi_m^h(z_h) \quad (9)$$

with the expansion coefficients $Y_{m,n}^{vc}(\rho, \omega)$. (In the following we will drop the argument ω for brevity.) Inserting the expansion into the interband equation (6), multiplying by $\psi_n^e \psi_m^h$, and integrating over the normal directions z_e and z_h yields a set of equations for the coefficients $Y_{m,n}^{vc}(\rho)$:

$$\sum_{m,n} \left[\left(\hbar(\omega_g - \omega - i\Gamma) + E_n^e + E_m^h - \frac{\hbar^2}{2\mu} \nabla_\rho^2 \right) \delta_{n,n'} \delta_{m,m'} + V_{n,n',m,m'}(\rho) \right] Y_{m,n}^{vc}(\rho) = M_{n',m'}^{vc}(\rho) \quad (10)$$

with the Coulomb matrix elements

$$V_{n,n',m,m'}(\rho) = -\frac{e^2}{4\pi\epsilon_0\epsilon} \int \int \frac{\psi_n^e(z_e) \psi_{m'}^h(z_h) \psi_n^e(z_e) \psi_m^h(z_h)}{\sqrt{\rho^2 + (z_e - z_h)^2}} dz_e dz_h \quad (11)$$

and the reduced in-plane mass $\mu = m_{e,\parallel} m_{h,\parallel} / (m_{e,\parallel} + m_{h,\parallel})$. Here the dipole matrix elements

$$M_{n,m}^{vc}(\rho) = \int \int \psi_n^e(z_e) \psi_m^h(z_h) M^{vc}(\rho, |z_e - z_h|) dz_e dz_h \quad (12a)$$

$$= \int \psi_n^e(Z) \psi_m^h(Z) dZ M_0 \frac{\delta(\rho - \rho_0)}{2\pi\rho_0} \quad (12b)$$

have been calculated by means of the shell model²²

$$M^{vc}(\rho, z) = M_0 \frac{\delta(\rho - \rho_0) \delta(z)}{2\pi\rho_0} \quad (13)$$

introducing the shell radius $\rho_0 = 2\sqrt{\hbar/(2\mu\omega_g)}$. Finally the resulting coefficients $Y_{mn}^{vc}(\rho)$, calculated for a finite shell radius ρ_0 , are extrapolated to the limit $\rho_0 \rightarrow 0$ according to the analytically known relation.¹⁹ This allows one to take into account correctly the singularity of both the Coulomb potential and dipole density for $\mathbf{r}=0$. From the complex-valued interband amplitude $Y^{vc}(\mathbf{R}, \mathbf{r}, \omega)$ the complex interband polarization

$$P(\mathbf{R}, \omega) = 2 \int M(\mathbf{r}) Y^{vc}(\mathbf{R}, \mathbf{r}, \omega) d^3\mathbf{r} \quad (14)$$

and the complex susceptibility

$$\chi(Z, \omega) = \frac{P}{\epsilon_0 E_\omega} = \frac{2M_0 Y^{vc}(Z, \omega)}{\epsilon_0 E_\omega} \quad (15)$$

can be calculated, where again the shell model has been used to reduce the integration. The susceptibility now depends only on Z because of the symmetry of the quantum well. Finally, the absorption coefficient is obtained from the susceptibility in Eq. (15) according to

$$\alpha(Z, \omega) = \frac{\omega}{cn_r} \text{Im} \frac{2M_0 Y^{vc}(Z, \omega)}{\epsilon_0 E_\omega}, \quad (16)$$

where c is the velocity of light and n_r is the real refractive index. Note that in Eq. (10) all Coulomb matrix elements are included.

As a consequence of the spatial inhomogeneity in the normal direction due to the electric field and the confinement potential, the polarization, and thus the absorption coefficient, emerge as functions of the center of mass coordinate Z . In the following, $\alpha(Z, \omega)$ is called the ‘‘local absorption coefficient,’’ and can be understood phenomenologically as the variation of the absorption coefficient resulting from the different materials of the heterostructure.

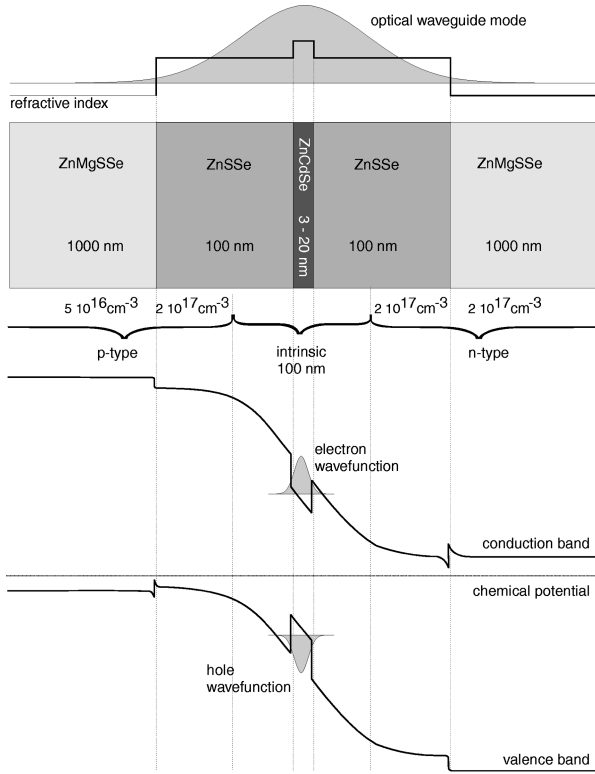


FIG. 1. Schematic sketch of a typical pin-waveguide structure with a single quantum well. The optical waveguide is formed by the ZnMgSSe cladding and the ZnS_xSe_{1-x} core. The quantum well is the Zn_yCd_{1-y}Se layer, embedded in the ZnS_xSe_{1-x} barrier. The band structure in thermodynamic equilibrium is schematically indicated in the bottom half. The intrinsic electric field at the quantum well is due to the space charge of the *pn* junction.

III. NUMERICAL RESULTS

A. Convergence

In this section we will solve Eq. (6) for the Zn_{0.7}Cd_{0.3}Se/ZnS_{0.06}Se_{0.94} quantum-well structure schematically shown in Fig. 1. The quantum well in those structures is under biaxial compressive strain, which leads to a splitting of the light- and heavy-hole bands by 86 meV. Hence, for the

calculation of the absorption coefficient in the vicinity of the band gap, only heavy holes have to be taken into account. As a consequence of the splitting, the heavy-hole dispersion relation can be approximated to be parabolic, and an effective mass can be defined. The diagonalization of the Luttinger Hamiltonian under strain was performed using standard methods (see Appendix A). The parameters used are listed in Table I.

The absorption coefficient is determined by means of a numerical solution of Eq. (10). First, the Coulomb matrix elements and the dipole matrix elements have to be calculated using the solutions of the one-dimensional electron and hole Schrödinger equations which have been obtained in Fourier space.²³

The energy spectrum of the Schrödinger equation for a quantum well in an electric field is continuous, with some resonances due to the levels in the well. The continuum can be turned into a quasicontinuum by placing the whole quantum-well structure in a sufficiently wide confining potential well with high barriers (here the width has been chosen as 60 nm).

For a numerical solution, expansion (9) must be truncated appropriately, depending upon the quantum-well width and the applied field. Figure 2 illustrates the wave functions included in the conduction and valence bands for a field of 80 kV/cm and a width of 15 nm. Equation (10) is solved using a standard discretization scheme in the spatial coordinate ρ .

In Fig. 3(a), the spatially averaged absorption coefficient for a 15-nm-wide quantum well is shown for photon energies ranging from the heavy-hole band edge at about 2.43 eV up to the energy gap of the ZnS_xSe_{1-x} barrier, which is at 2.72 eV. The various curves differ by the number of wave functions N taken into account in each band. As expected, an additional excitonic resonance peak is found for each extra pair of wave functions included. In addition, it can be seen that the inclusion of a further pair of wave functions enhances the resonance peak of *other* resonances. This clearly shows the importance of the Coulomb coupling between different sublevels. Nevertheless, the convergence is extremely fast. In the vicinity of the heavy-hole band edge, good convergence is already achieved with $N=6$, i.e., a total of 12 wave functions. In order to demonstrate the convergence

TABLE I. Material parameters used for the calculations. The Luttinger parameters are interpolated from the parameters given in Ref. 36 for the binary alloys. The elastic stiffness and deformation potentials and the effective electron masses are interpolated from the parameters given in Refs. 37–39.

band gap of barrier material (ZnS _{0.06} Se _{0.94})	2.72 eV
band gap of well material (Zn _{0.7} Cd _{0.3} Se)	2.40 eV
resulting conduction-band offset (without strain)	256 meV
resulting valence-band offset (without strain)	64 meV
effective electron mass m_e of Zn _{0.7} Cd _{0.3} Se/ZnS _{0.06} Se _{0.94}	(0.14/0.15) m_0
Luttinger parameters $\gamma_1 / \gamma_2 / \gamma_3$ of Zn _{0.7} Cd _{0.3} Se	3.21/1.01/2.20
Luttinger parameters $\gamma_1 / \gamma_2 / \gamma_3$ of ZnS _{0.06} Se _{0.94}	3.15/0.735/1.97
elastic stiffness C_{11}/C_{12}	7.78/4.88 N/m ²
hydrostatic deformation potential a	-4.07 eV
shear deformation potential b	-1.08 eV
exciton-phonon linewidth Γ	10 meV
relative permittivity ϵ	8.7
doping concentration (p-type/n-type)	$2 \times 10^{17} \text{ cm}^{-3}$

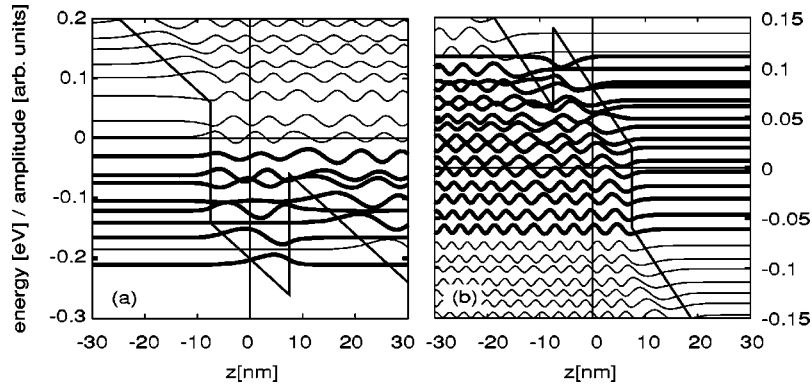


FIG. 2. Calculated wave functions of (a) conduction band and (b) valence band of a 15-nm-wide quantum-well structure in an applied electric field of $F=80$ kV/cm. The thick lines represent those wave functions which were included in the expansion of the interband amplitude Y^{vc} .

properties in Fig. 3 the absorption coefficient is shown for energies ranging from the quantum-well band gap to the band gap of the barrier material. Note that the light holes can be neglected for energies near the quantum-well band gap, but need to be included for higher energies. Further, the bulk exciton in the $\text{ZnS}_x\text{Se}_{1-x}$ barrier material starts to develop at the high-energy side, although more than 12 wave functions would be necessary to fully resolve the peak.

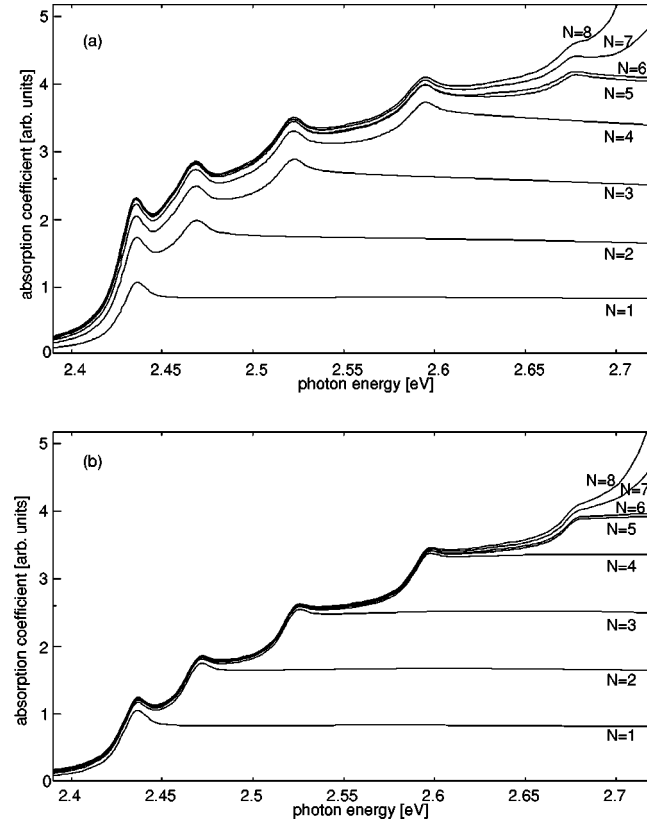


FIG. 3. Calculated absorption coefficient as a function of photon energy ($F=0$, $L^{QW}=15$ nm). (a) Full model. (b) Reduced model where only diagonal Coulomb matrix elements are used. The convergence is demonstrated by comparing different curves corresponding to a different number of wave functions in the conduction band N and in the valence band N included in the expansion of the interband amplitude.

We have compared the solution of the full model [Fig. 3(a)] with a reduced model where the Coulomb interaction between different levels within the same quantum well is neglected (see Appendix B). The resulting convergence of the expansion is shown in Fig. 3(b). Differences between both diagrams must be attributed to the coupling between different levels of the same band. From Fig. 3(b) it can be deduced that—in contrast to the full model—the inclusion of a further pair of levels does not alter the absorption spectrum for photon energies below the resonance energy $E_g + E_n + E_m$, where E_n and E_m are the energies of the respective levels. Hence it is evident that the simple model must not be used if the dielectric constant is small and excitonic effects are important. However, the reduced model is sufficient for materials with weak excitonic effects, e.g., GaAs/Al_xGa_{1-x}As heterostructures.²⁴

B. Absorption coefficient

Here we consider an experimental setup where the light is transmitted vertically through the quantum-well structure. If the absorption coefficient α is constant along the propagation direction, the optical power $P(Z) = P_0 \exp(-\alpha Z)$ is exponentially attenuated. Generalizing this to a spatially dependent absorption coefficient $\alpha(Z)$,

$$\frac{dP(Z)}{dZ} = -\alpha(Z)P(Z), \quad (17)$$

we obtain the solution

$$P_{out} = P_{in} \exp\left(-\int_{-L^z/2}^{+L^z/2} \alpha(z') dz'\right), \quad (18)$$

which relates the output power $P_{out} = P(Z = +L^z/2)$ to the input power $P_{in} = P(Z = -L^z/2)$ for a symmetric sample with surfaces at $Z = \pm L^z/2$. The absorption coefficient, varying on a nanometer scale, thus enters the expression for the transmitted optical power in an integrated form. With the definition of an absorption coefficient integrated over the propagation direction and normalized by the width L^{QW} of the quantum well according to

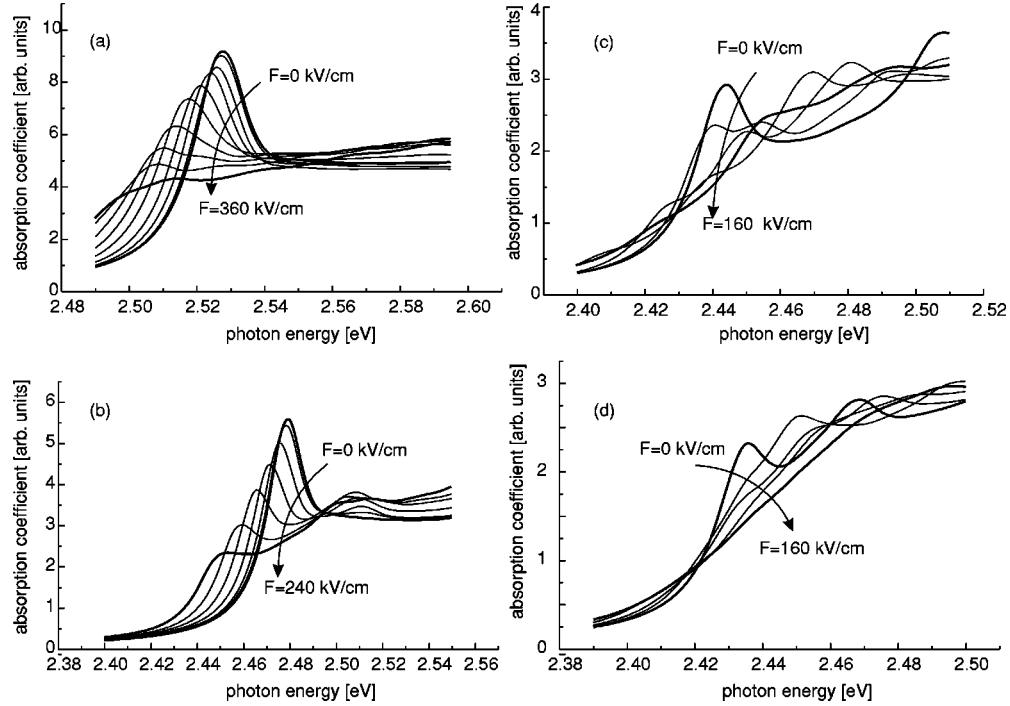


FIG. 4. Calculated electric-field dependence of the absorption coefficient α^{QW} for different widths of the $\text{Zn}_y\text{Cd}_{1-y}\text{Se}$ quantum well: (a) 3 nm, (b) 5 nm, (c) 10 nm, and (d) 15 nm. Different curves correspond to different electric-field strengths increasing with the arrow in steps of 40 kV/cm (for numerical parameters, see Table I; $\Gamma = 10$ meV).

$$\alpha^{QW} = \frac{1}{L^{QW}} \int_{-L^Z/2}^{+L^Z/2} \alpha(z') dz', \quad (19)$$

the output power is

$$P_{out} = P_{in} e^{-\alpha^{QW} L^{QW}}. \quad (20)$$

As the absorption coefficient cannot be spatially resolved in experiments, the calculated local absorption coefficient $\alpha(Z)$ has to be related to the measured absorption coefficient α^{QW} according to Eq. (19).

Now the numerical results of the absorption coefficient α^{QW} as defined by Eqs. (19) and (16) will be presented. We have performed simulations for $\text{Zn}_y\text{Cd}_{1-y}\text{Se}$ quantum wells with a width of $L^{QW} = 3, 5, 10,$ and 15 nm and different applied electric fields. Starting from a nearly two-dimensional situation, Fig. 4(a) shows the (averaged) absorption coefficient α^{QW} for a well width of 3 nm for fields up to 360 kV/cm (in steps of 40 kV/cm in the direction of the arrow). The field-dependent changes can obviously be attributed to the *quantum-confined Stark effect*. With increasing field the excitonic resonance shifts to lower photon energies accompanied by a strong decrease in the peak value together with a field-induced broadening of the peak width. At about 360 kV/cm the excitonic peak disappears, and the absorption coefficient is reduced approximately to half of the peak value at zero field. At energies below the zero-field absorption edge, the absorption coefficient increases approximately by a factor of 3.

For the 5-nm quantum well, the simulation results are depicted in Fig. 4(b). Again, the quantum-confined Stark effect can clearly be identified by the peak shift as well as by the decrease of the peak value. On the high-energy shoulder, an additional peak arises with increasing electric field. While

the absorption peak at zero-field is due to the hole ground state to electron ground-state transition, this new peak is caused by transitions from the second level of the hole to the ground state of the electron. This additional transition is forbidden at zero field because of parity reasons. With increasing electric field, the wave functions become distorted, and hence the overlap of the wave functions involved in the forbidden transitions does not vanish any more. Note that with increasing field the transition of the second electron level to the first hole level also becomes an allowed transition, but lies at slightly higher energies because of the effective mass ratio as well as the different band discontinuities.

Besides the appearance of the new peak, a comparison of the results for the 3- and 5-nm quantum well shows that the electric-field-induced broadening of the resonance peak is more pronounced for the wider well. This is fully in accordance with the interpretation of the quantum-confined Stark effect: the barriers of the quantum well prevent the distortion (dissociation) of the exciton due to the electric field, which is more effective for a narrow well.

Now looking at the results for the 10-nm quantum well, plotted in Fig. 4(c), the zero-field curve shows a second peak at the high-energy side which is due to allowed transitions from the second hole level to the second electron level. With increasing electric field, both resonance peaks rapidly become broadened, although a very small shoulder shifting to lower energies can be seen. Again, other (forbidden) transitions emerge with increasing field. Moreover, at 10 nm the intersubband spacing is reduced in comparison with smaller wells. Therefore, the number of transitions involved in the absorption process is increased. Further, the different peaks can no longer be attributed to specific transitions, due to the Coulomb coupling of the different sublevels. However, the

spectrum exhibits resonances if the photon energy matches the energy separation of a particular electron-hole sublevel pair. From the dependence of the absorption coefficient on the electric-field strength, it can be deduced that the well width of 10 nm corresponds to the transition from a two-dimensional to a three-dimensional behavior of the absorption coefficient: The spectra show excitonic peaks (even at 120 kV/cm a small resonance peak can be found, at least for a linewidth of $\Gamma = 10$ meV which is used throughout); however, a pronounced redshift cannot be found due to a rapid field-induced dissociation of the exciton, which results in a strong broadening of the resonances with increasing electric field.

For a quantum-well width of 15 nm, the results shown in Fig. 4(d) indicate that bulklike behavior with respect to the dimensionality of the exciton is found. The excitonic peak at zero field vanishes before any peak shift can be seen. At 160 kV/cm, the spectrum is monotonic. However, with respect to the density of states, the bulk limit is not reached, and hence the absorption spectra for the 15-nm quantum well can be associated with the *quantum-confined Franz-Keldysh regime*. The investigation of a wider well, e.g., of 20-nm width, would correspond to the transition from a two- to a three-dimensional center-of-mass motion. This, however, cannot be seen in absorption spectra, since momentum conservation requires a vanishing center-of-mass motion. Thus the results for a 20-nm well do not provide any further information. Moreover, due to the slower convergence of the series expansion of the interband amplitude, the computational effort will increase tremendously.

In summary, for all well widths investigated here, a strong electric-field-induced decrease in the absorption coefficient at the excitonic resonance and a substantial increase below the excitonic resonance was found. The electric-field strength necessary to broaden the resonance significantly is much higher for narrower wells. However, it should be pointed out that an important parameter which has a significant impact on the result is the linewidth Γ originating from the exciton-phonon coupling which, in turn, strongly depends on the well width. A microscopic analysis of the well width dependence of the linewidth²⁵⁻²⁷ is outside the scope of this paper. The measured exciton-LO-phonon coupling parameters²⁸ lead to the conclusion that the linewidth is of the order of $\Gamma \approx 10$ meV for a 3-nm quantum well at room temperature, and of the order of $\Gamma \approx 20$ meV for a 10-nm quantum well at room temperature. Generally, two effects compete in the well width dependence of the absorption coefficient: the electric-field dependence originating from the dimensionality of the Coulomb interaction, as discussed above, and the well width dependence of the exciton-phonon interaction manifested in the linewidth. In order to clearly separate these two effects and to give prominence to the “dimensionality-induced” transition, the linewidth has been set to a constant value of $\Gamma = 10$ meV in all our calculations. While this value is expected to be a good estimate for narrow wells, it slightly underestimates the exciton-phonon interaction for wide wells. However, this choice enables the identification of the Stark shift which would be smoothed out otherwise in our simulations. Due to this assumption, for all well widths a pronounced absorptive electro-optical effect is found.

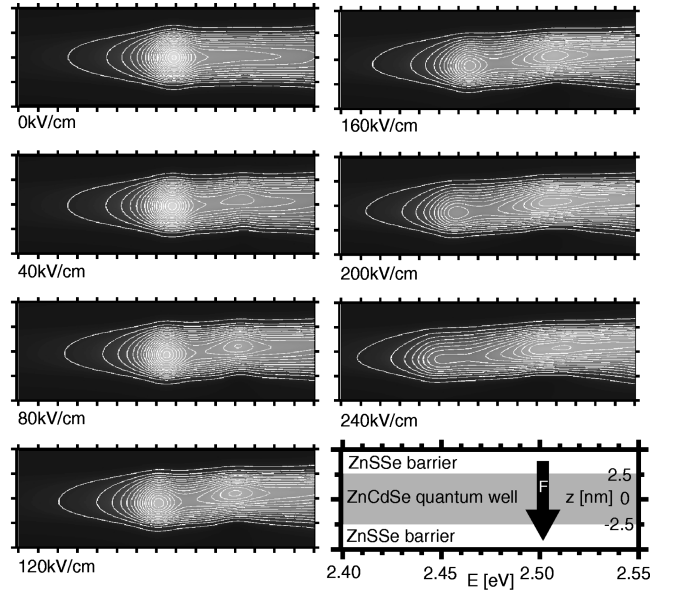


FIG. 5. Density plot of the local absorption coefficient $\alpha(Z, \omega)$ for a 5-nm quantum well for different electric fields. The energy ($E = \hbar\omega$) and space (Z) scales and the direction of the electric field F (arrow) are shown on the bottom right scheme. Additionally, contour lines are given as a guide to the eye.

C. Spatially resolved absorption spectra

Our quantum-mechanical theory in fact provides even more detailed information than has been used in Sec. III B, where the integrated absorption coefficient was presented. In this section, the spatially resolved or *local* absorption coefficient $\alpha(Z, \omega)$ [Eq. (16)], which depends upon the normal component of the center-of-mass coordinate Z , will be discussed.

At this point, it should be noted that the local absorption coefficient emerges from a quantum-mechanical treatment of the polarization. Thus the local absorption coefficient is a microscopic quantity. This is emphasized by the expansion of the polarization using the solutions of the one-dimensional Schrödinger equation as the basis in Eq. (9). Here the local absorption coefficient $\alpha(Z, \omega)$ can be used to identify and visualize the origin of the various peaks in the integrated absorption coefficient α^{QW} .

In the following, the local absorption coefficient $\alpha(Z, \omega)$ is visualized as a density plot, where bright colors refer to large values. As a guide to the eye, equidistant contour lines are additionally supplied. In Fig. 5, $\alpha(Z, \omega)$ is plotted for a quantum well of 5-nm width. At zero field, the excitonic resonance is clearly visible. With an electric field, the first forbidden transition becomes weakly allowed (40 kV/cm). This is the small peak which also appears in Fig. 4(b). With increasing electric field, the peak of the fundamental resonance decreases due to reduced overlap of the wave functions, and the forbidden transition becomes more visible and eventually dominates the allowed peak (200 kV/cm). Finally, at 240 kV/cm, the peak structure is almost completely lost, and the absorption coefficient increases monotonically with the photon energy.

At zero field, the local absorption coefficient is symmetric with respect to the center of the quantum well. Owing to the different effective masses of electrons and holes as well as

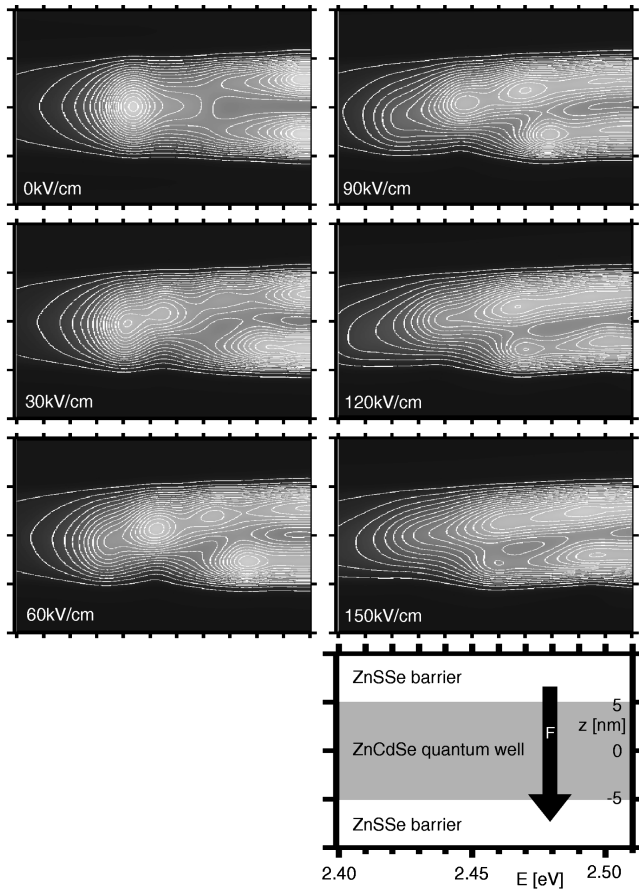


FIG. 6. Same as Fig. 5 for a 10-nm quantum well.

due to the different depths of the conduction- and valence-band quantum wells, the symmetry is lost with increasing applied electric field. In the subfigures above 120 kV/cm, this is clearly visible. For photon energies in the vicinity of the fundamental resonance, the (first) peak of the spatially resolved absorption coefficient is shifted in the direction of the electric field. For higher photon energies, the (second) peak of the local absorption coefficient is shifted against the direction of the electric field. Since the effective mass of the heavy holes is significantly larger than the effective mass of the electrons, and since the conduction-band quantum well is significantly deeper than the valence-band well, this can be interpreted in terms of a distorted hole wave function: The hole ground-state wave function is pushed into the direction of the electric field, whereas the first excited wave function is distorted in the opposite direction.

In the case of the 10-nm quantum well, for which the results are given in Fig. 6, the zero-field subfigure shows the emergence of the second allowed transition at the high-energy side of the spectrum. Here again the properties of the underlying wave functions are recovered: The first allowed transition, which is related to the pair of the first (i.e., ground state) quantum-well wave functions, yields a single peak in the local absorption coefficient. The second allowed transition is related to the pair of the second (i.e., first excited) wave functions of the conduction- and valence-band quantum wells, respectively. Due to the uneven parity of the first excited wave functions, the local absorption coefficient splits into two spatially (in the Z direction) separated peaks. With

increasing applied electric field, the forbidden transitions arise between the resonances of the allowed transitions, and subsequently merge with those with concomitant asymmetries in the Z direction.

IV. COMPARISON WITH EXPERIMENTS

The theoretical results presented in Sec. III will now be compared with measurements of ZnSe-based heterostructures. The samples are similar to the schematic structure sketched in Fig. 1; however, the ZnMgSSe waveguide cladding layers are missing since the structures were not intended for waveguide transmission experiments. This does not restrict the validity of a comparison of experimental and theoretical results. We have used photocurrent spectroscopy to obtain absorption spectra of these p - i - n diodes with different quantum wells embedded in the intrinsic region of the diode. The structures were illuminated with monochromatic light obtained from a low-noise Xe lamp in conjunction with a monochromator. Since the quantum well is included in the intrinsic region ($z_i \leq 360$ nm), even without applied external voltage the electric field is of the order of 100–200 kV/cm. This field strength leads to an effective carrier separation and a quantum efficiency close to 1.²⁹ By applying an external bias voltage to the samples, we are able to increase or decrease the field strength in the quantum-well region. The absorption coefficient α can be calculated from the photocurrent J by the relation

$$J = -e(1-R) \frac{P}{\hbar\omega} \alpha L^{QW}, \quad (21)$$

where P is the excitation power, and R is the reflectivity of the surface. This equation is only valid if the electric field is effectively separating the carriers, which prevents the use of this method for low electric fields.

The samples were grown by molecular beam epitaxy at the University of Bremen on n -doped GaAs substrates with GaAs buffer layers to improve the crystalline quality of the overall structure. All II-VI layers, with the exception of the quantum well, were made of $\text{ZnS}_x\text{Se}_{1-x}$ ($x \sim 0.06$) and lattice matched to GaAs at room temperature. This composition was chosen to reduce the creation of lattice defects due to relaxation of the II-VI layers, which would lead to an increased dark current during the photocurrent measurements. The doping of the p and n layers is approximately $2 \times 10^{17} \text{ cm}^{-3}$, with the p layer on top of the whole structure. Gold was used to generate the contacts on top of the samples. This material leads to non-Ohmic contacts, and prevents a direct correlation between the applied voltage and the internal electric field. The quantum wells were placed in the middle of the intrinsic layer and are composed of $\text{Zn}_y\text{Cd}_{1-y}\text{Se}$ with a Cd content between 20% and 25%. This amount of Cd allows the growth of layers with a maximum thickness of 20 nm without the formation of misfit dislocations. These defects would lead to increased nonradiative recombination of the photocarriers, and prevent a direct correlation of the current with the absorption coefficient. It should be noted that the cadmium content in the theoretical calculations was chosen to be 30%, which represents the upper limit for Cd in electro-optic devices and leads to higher confinement and higher strain effects within the quan-

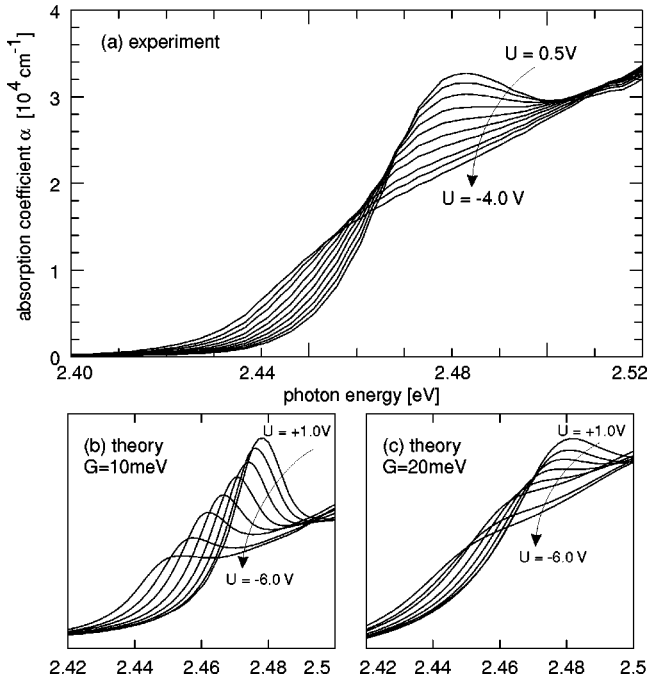


FIG. 7. (a) Measured absorption coefficient for a multiple quantum well (four periods of $L^{QW}=5$ nm) for different applied voltages decreased from $U=+0.5$ to $U=-4.0$ V in steps of 0.5 V. For comparison, the results of the simulations are given for (b) $\Gamma=10$ meV and (c) $\Gamma=20$ meV.

tum well. However, the weaker confinement in the experimental structures causes a smaller level spacing within the quantum well, and enhances the influence of the Coulomb coupling effects. The overall comparability of the experiment and theory is well given in spite of the small deviations of the Cd content. In Fig. 7(a), the measured absorption coefficient is plotted for a 5-nm multiple quantum well with a Cd content of 20%, which is embedded in an intrinsic layer of 360-nm thickness. Curves are shown for different voltages in the range from $U=+0.5$ V to $U=-4$ V. For the low-field case, the quantum-well absorption exhibits a peak which is fully broadened with increasing reverse bias. Although no pronounced shift of the peak energy can be detected, the behavior can be classified as belonging to the quantum-confined Stark effect regime, since the excitonic resonance is preserved up to high fields ($U=0$ must be attributed to the high-field regime due to the large built-in voltage resulting from the doping). For comparison, in Fig. 7(b), the results of the simulation using a linewidth of $\Gamma=10$ meV, corresponding to Fig. 4(b), are shown. Here the field strength F is converted into a device voltage U using the simple relation $F=(U_{bi}-U)/z_i$ with the built-in voltage $U_{bi}=2.57$ V and the width of the intrinsic layer $z_i=360$ nm. Further, Fig. 7(c) shows the same calculations but with $\Gamma=20$ meV. Comparing the experimental peak width with the simulations one can estimate the linewidth to be of the order of $\Gamma\approx 20$ meV (at room temperature). Good overall agreement of experiment and theory is found.

Figure 8 shows the measured absorption coefficient for a single quantum well with a width of 10 nm. The cadmium content was 25%, and the thickness of the intrinsic layer was 200 nm. For the applied voltage range, corresponding to extremely high fields up to 250 kV/cm, no excitonic resonances

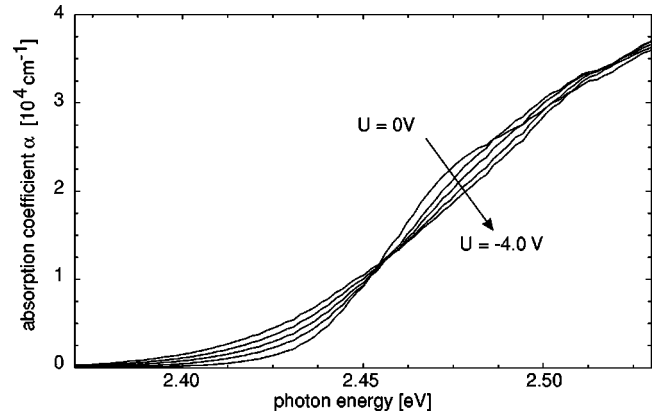


FIG. 8. Measured absorption coefficient for a 10-nm (single) quantum well for voltages $U=0$ to $U=-4$ V.

are found, and the spectrum shows the characteristic features related with the Franz-Keldysh effect, i.e., a decrease of the absorption close to the band edge and an increase for lower photon energies. This can also be observed in a single quantum well with a thickness of 20 nm. Nevertheless, the Coulomb interaction is still important, and leads to a very steep absorption edge in spite of the high built-in electric field in the intrinsic layer of the order of 120 kV/cm at zero bias voltage. A direct comparison with the theoretical results is more difficult here, since our model was specifically designed for the transition regime and the computational effort to reach comparably high fields for wide quantum wells would be tremendous. The theoretical results indicate that the Franz-Keldysh regime is reached at moderate field strength, which is in full accordance with the experiments.

V. CONCLUSIONS

The main objective of this paper is to discuss the electric field dependence of electroabsorptive effects in $\text{Zn}_y\text{Cd}_{1-y}\text{Se}/\text{ZnS}_x\text{Se}_{1-x}$ quantum-well structures of different well widths. Because of much stronger Coulomb effects, the scenario of the transition from two-dimensional to bulk behavior in wide-gap materials is entirely different from that in $\text{GaAs}/\text{Al}_x\text{Ga}_{1-x}\text{As}$ structures, where it reflects the dependence of the density of states upon the quantum-well width. Strong Coulomb interaction results in a significant exciton binding energy and, thus, in a small exciton Bohr radius. Hence strong modifications of the electric-field dependence of the absorption spectra can be expected if the well width is larger than the diameter of the exciton. Already at well widths where the density of states in the quantum well is far from being bulklike, a transition occurs. It can be related to a change in the dimensionality of the quantum-well exciton: A well width smaller than the (bulk) exciton diameter results in a two-dimensional exciton, i.e., the relative motion of the electron-hole pair is confined to the well plane. If the well width approximately matches the (bulk) exciton diameter, the relative motion is essentially three dimensional, whereas the center-of-mass motion is still restricted to the plane of the quantum well. Thus the important quantity for the distinction of the different regimes is the bulk exciton Bohr radius.

With respect to the electric-field dependence of the ab-

sorption coefficient, it has been found that the *quantum-confined Stark effect* occurs for very narrow wells. For wells of the order of the above-defined transition regime, the spectra show a (conventional, not quantum-confined) excitonic Stark effect, i.e., an exciton peak at zero field which rapidly disappears if an electric field is applied. This effect is due to the field-induced polarization and subsequent dissociation of the exciton (since the electric field distorts the electron and hole wave functions in opposite directions), while the shift of the excitonic peak (Stark shift) is rather insignificant. In other words, the main effect of the electric field is that it reduces the lifetime of the exciton (with respect to dissociation, not recombination), leading to a broadening of the excitonic peak in absorption. This broadening exceeds the energy shift induced by the electric field. A bulklike situation (Franz-Keldysh effect) is recovered at much larger well widths. In view of applications for room-temperature operation, the well width should be chosen such that it results in a minimum exciton-phonon coupling in order to minimize the temperature-induced broadening of the excitonic peak. The general trend is that the coupling parameter increases with the well width; thus narrow wells are favorable.

Finally, our theoretical treatment, which is based on the density-matrix formalism in real space and fully accounts for the Coulomb interaction, allows for a simulation of the spatially resolved, local absorption coefficient. It has been used for a detailed explanation of the origin of the various peaks found in the integrated absorption coefficient. The integrated absorption coefficient, which is the quantity observed experimentally, can thereby be related to quantum-mechanical features. Good agreement between theory and experiment has been found. Since the difference between conventional models and the advanced model developed here are physically caused by the strong Coulomb coupling typical for wide-gap materials with a small dielectric constant, we suggest that our advanced model applies not only to $\text{Zn}_y\text{Cd}_{1-y}\text{Se}/\text{ZnS}_x\text{Se}_{1-x}$ structures, but to a much larger class of wide-gap materials. It offers the convenient possibility to treat a wide range of well widths up to very high electric fields.

The physical interest in these structures is strongly motivated by their potential application as modulators and switches in integrated optoelectronics in the blue-green range. Indeed, the pronounced field dependence of the absorption coefficient found in this work may be used in self-electro-optic effect devices. The occurrence of electro-optic bistability can be demonstrated based on the obtained electroabsorption spectra.^{30,31} These phenomena will be elaborated in further studies.

ACKNOWLEDGMENTS

We are grateful to R. Zimmermann for enlightening discussions and to D. Hommel, M. Behringer, and M. Fehrer for preparation of the samples. This work was supported by DFG.

APPENDIX A: LUTTINGER HAMILTONIAN FOR HOLES IN STRAINED QUANTUM WELLS

The valence band in zinc-blende semiconductors is formed by three states with an orbital angular momentum

$L=1$ with $m_L=0, \pm 1$. Because of the spin-orbit coupling, this results in six eigenstates of $\mathbf{J}=\mathbf{L}+\mathbf{s}$. The states with $J=\frac{1}{2}$ and $m_J=\pm\frac{1}{2}$ form the split-off band (Γ_7 symmetry), while the states with $J=\frac{3}{2}$ build the highest-lying valence band having Γ_8 symmetry. In bulk semiconductors, the heavy and light holes are degenerate at $k=0$. The reduction of symmetry in quantum wells leads to a splitting such that the heavy-hole energy band lies above the light-hole band.

If the materials forming the quantum well and barriers have different lattice constants, the quantum well becomes biaxially strained. As a result, the in-plane valence-band dispersion is modified.^{32,33} The *hydrostatic* component δE_{hy} of the strain only shifts the bands energetically, i.e., it modifies the band gap of the strained quantum well. It is assumed³³ that the shift due to the hydrostatic component of the strain applies with a ratio of $\frac{2}{3}:\frac{1}{3}$ to the conduction and valence bands, respectively. The *shear* component δE_{sh} also modifies the total band gap, but only affects the hole subbands. In particular, the effect of the shear contribution is a (further) splitting of the light- and heavy-hole bands. With the inclusion of strain, the Luttinger Hamiltonian becomes the Pikus-Bir Hamiltonian, which may be unitarily transformed into a block diagonal form³⁴

$$\mathcal{H}^\sigma = \begin{pmatrix} P \pm Q \pm \delta E_{hy}/2 & |R| - i|S| \\ |R| + i|S| & P \mp Q \mp \delta E_{hy}/2 \end{pmatrix}, \quad \sigma = U, L, \quad (\text{A1})$$

where σ labels the upper (U) and lower (L) blocks of the Hamiltonian corresponding to the in-plane dispersion relation for the heavy and light holes, respectively, and

$$P = \frac{\hbar^2}{2m_0} \gamma_1 (k_x^2 + k_y^2 + k_z^2) + V(z), \quad (\text{A2a})$$

$$Q = \frac{\hbar^2}{2m_0} \gamma_2 (k_x^2 + k_y^2 - 2k_z^2), \quad (\text{A2b})$$

$$S = \sqrt{3} \frac{\hbar^2}{m_0} \gamma_3 k_z (k_x - ik_y), \quad (\text{A2c})$$

$$R = -\frac{\hbar^2}{m_0} \left(\frac{\sqrt{3}}{4} (\gamma_2 + \gamma_3) (k_x - ik_y)^2 - \frac{\sqrt{3}}{4} (\gamma_3 - \gamma_2) (k_x + ik_y)^2 \right), \quad (\text{A2d})$$

where $V(z)$ is the quantum well potential.

For the $\text{Zn}_y\text{Cd}_{1-y}\text{Se}/\text{ZnS}_x\text{Se}_{1-x}$ structures investigated here, the total band-gap discontinuity of the $\text{Zn}_y\text{Cd}_{1-y}\text{Se}/\text{ZnS}_x\text{Se}_{1-x}$ structure is 320 meV (cf. Table I). Assuming a ratio of 80:20 for the contribution to the conduction and valence bands, the conduction-band offset is 256 meV and the valence-band offset is 64 meV. The different lattice constants for the well and barrier materials lead to a biaxial compression of the well, resulting in strain-induced changes of the band gap. The hydrostatic component of the strain is evaluated as $\delta E_{hy} = -81$ meV, which gives a conduction-band offset of 202 meV and a valence-band off-

set of 37 meV. The shear component of the strain is $\delta E_{sh} = -86$ meV, splitting the heavy- and light-hole bands. While the heavy-hole band offset is increased by $-\delta E_{sh}/2$ to a value of 80 meV, the light-hole offset is decreased to -6 meV. This means that the light holes are anticonfined, i.e., the $\text{Zn}_y\text{Cd}_{1-y}\text{Se}$ layer forms a barrier for light holes (cf. similar type-II quantum-well structures in the $\text{Zn}_y\text{Cd}_{1-y}\text{Se}/\text{ZnSe}$ system³⁵).

We have calculated the in-plane valence-band dispersion relation from the Hamiltonian equation (A1) for different quantum-well widths. Our results show that the heavy-hole valence band is parabolic to a good approximation, and that the resulting effective mass decreases monotonically with the width.³¹

APPENDIX B: COMPARISON WITH A REDUCED MODEL

A reduced model can be obtained from Eq. (10) by replacing the Coulomb matrix elements in Eq. (11) with

$$V_{n,n',m,m'}^r(\rho) = V_{n,n',m,m'}(\rho) \delta_{n,n'} \delta_{m,m'} \quad (\text{B1a})$$

$$= -\frac{e^2}{4\pi\epsilon_0\epsilon} \int \int \frac{|\psi_n^e(z_e)|^2 |\psi_m^h(z_h)|^2}{\sqrt{\rho^2 + (z_e - z_h)^2}} dz_e dz_h. \quad (\text{B1b})$$

In the reduced model, the Coulomb potential couples electrons attributed to sublevel n with holes attributed to sublevel m , but the coupling between various electron levels as well as the coupling between various hole levels is neglected. Hence Eqs. (10) become decoupled,

$$\left(\hbar(\omega_g^{nm} - \omega - i\Gamma) - \frac{\hbar^2}{2\mu} \nabla_\rho^2 + V_{n,m}^r(\rho) \right) Y_{nm}^{red}(\rho) = M_{nm}(\rho), \quad (\text{B2})$$

with $\hbar\omega_g^{nm} = \hbar\omega_g + E_n^e + E_m^h$, and can be solved by a series expansion into solutions of the corresponding homogeneous eigenvalue problem

$$\left(-\frac{\hbar^2}{2\mu} \nabla_\rho^2 + V_{nm}^r \right) Y_{nm}^{red,i} = E_{nm}^i Y_{nm}^{red,i}. \quad (\text{B3})$$

This eigenvalue problem is the standard Schrödinger equation of an exciton formed by an electron and a hole, both described by particular wave functions $\psi^e(z_e)$ and $\psi^h(z_h)$, respectively. This independent subband approximation is equivalent to the simpler models generally used, e.g., for GaAs/Al_xGa_{1-x}As structures.²⁴ In ZnSe-based structures, however, due to the strong Coulomb interaction, coupling of different levels within the same quantum well becomes essential (cf. Fig. 3).

-
- ¹M. A. Haase, J. Qiu, J. M. DePuydt, and H. Cheng, *Appl. Phys. Lett.* **59**, 1272 (1991).
- ²M. A. Haase, H. Cheng, D. K. Misemer, T. A. Strand, and J. M. DePuydt, *Appl. Phys. Lett.* **59**, 3228 (1991).
- ³A. L. Ivanov, H. Haug, S. Knigge, and D. Jäger, *Jpn. J. Appl. Phys., Suppl.* **34**, 15 (1995).
- ⁴W. Franz, *Z. Naturforsch. A* **13A**, 484 (1958).
- ⁵L. V. Keldysh, *Zh. Eksp. Teor. Fiz.* **34**, 1138 (1958) [*Sov. Phys. JETP* **34**, 788 (1958)].
- ⁶K. W. Böer, H. J. Hänsch, and U. Kümmel, *Z. Phys.* **135**, 170 (1959).
- ⁷D. A. B. Miller, D. S. Chemla, T. C. Damen, A. C. Gossard, W. Wiegmann, T. H. Wood, and C. A. Burrus, *Phys. Rev. Lett.* **53**, 2173 (1984).
- ⁸*Theory of Transport Properties of Semiconductor Nanostructures*, edited by E. Schöll (Chapman and Hall, London, 1998).
- ⁹S. Y. Wang, G. Horsburgh, P. Thompson, I. Hauksson, J. T. Mullins, K. A. Prior, and B. C. Cavenett, *Appl. Phys. Lett.* **63**, 857 (1993).
- ¹⁰P. V. Giugno, M. D. Vittorio, R. Rinaldi, R. Cingolani, F. Quaranta, L. Vanzetti, L. Sorba, and A. Franciosi, *Phys. Rev. B* **54**, 16934 (1996).
- ¹¹D. A. B. Miller, D. S. Chemla, and S. Schmitt-Rink, *Phys. Rev. B* **33**, 6976 (1986).
- ¹²R. J. Elliot, *Phys. Rev.* **108**, 1384 (1957).
- ¹³M. Shinada and S. Sugano, *J. Phys. Soc. Jpn.* **21**, 1936 (1966).
- ¹⁴P. Lefebvre, P. Christol, and H. Mathieu, *J. Phys. IV* **3**, 377 (1993).
- ¹⁵P. Lefebvre, P. Christol, and H. Mathieu, *Superlattices Microstruct.* **17**, 19 (1995).
- ¹⁶R. Zimmermann, *Jpn. J. Appl. Phys., Suppl.* **34**, 228 (1995).
- ¹⁷D. A. B. Miller, D. S. Chemla, T. C. Damen, A. C. Gossard, W. Wiegmann, T. H. Wood, and C. A. Burrus, *Phys. Rev. B* **32**, 1043 (1985).
- ¹⁸P. J. Mares and S. L. Chuang, *J. Appl. Phys.* **74**, 1388 (1993).
- ¹⁹A. Stahl and I. Balslev, *Electrodynamics of the Semiconductor Band Edge* (Springer, Berlin, 1987).
- ²⁰I. Balslev, R. Zimmermann, and A. Stahl, *Phys. Rev. B* **40**, 4095 (1989).
- ²¹A. Stahl, *Phys. Status Solidi B* **159**, 327 (1990).
- ²²A. Stahl and I. Balslev, *Phys. Status Solidi B* **113**, 583 (1982).
- ²³D. L. Mathine, S. K. Myjak, and G. N. Maracas, *IEEE J. Quantum Electron.* **31**, 1216 (1995).
- ²⁴H. Mikkelsen, *Optoelectronic Modulators in Bulk, Multiple Quantum Well and Superlattice Semiconductor Structures, Berichte aus der Halbleitertechnik* (Shaker, Aachen, 1994).
- ²⁵S. Rudin, T. L. Reinecke, and B. Segall, *Phys. Rev. B* **42**, 11218 (1990).
- ²⁶S. Rudin and T. L. Reinecke, *Phys. Rev. B* **41**, 3017 (1990).
- ²⁷P. M. Young, E. Runge, M. Ziegler, and H. Ehrenreich, *Phys. Rev. B* **49**, 7424 (1994).
- ²⁸N. T. Pelekanos, J. Ding, M. Hagerott, A. V. Nurmikko, H. Luo, N. Samarth, and J. K. Furdyna, *Phys. Rev. B* **45**, 6037 (1992).
- ²⁹W. Ebeling, B. S. Ryvkin, J. Gutowski, K. Schüll, B. Jobst, and D. Hommel, *J. Cryst. Growth* **159**, 893 (1996).
- ³⁰W. Ebeling, D. Merbach, M. Behringer, M. Fehrer, P. Michler, J. Gutowski, E. Schöll, and D. Hommel, *J. Cryst. Growth* **184/185**, 706 (1998).
- ³¹D. Merbach, Ph.D. thesis, Technical University of Berlin, 1998.
- ³²D. Ahn and S. L. Chuang, *IEEE J. Quantum Electron.* **30**, 350 (1994).
- ³³S. L. Chuang, *Phys. Rev. B* **43**, 9649 (1991).

- ³⁴D. Ahn, S. L. Chuang, and Y.-C. Chang, *J. Appl. Phys.* **64**, 4056 (1988).
- ³⁵C. Guénaud, E. Deleporte, A. Filoramo, P. Lelong, C. Delalande, C. Morhain, E. Tournié, and J. P. Faurie, *J. Cryst. Growth* **184/185**, 839 (1998).
- ³⁶M. Willatzen, M. Cardona, and N. E. Christen, *Phys. Rev. B* **51**, 17 992 (1995).
- ³⁷H. J. Lozykowski and V. K. Shastri, *J. Appl. Phys.* **69**, 3235 (1991).
- ³⁸N. Tomassini, A. D. Andrea, G. Martino, R. Girlanda, and R. Atanasov, *Phys. Rev. B* **52**, 11 113 (1995).
- ³⁹S. Lankes, M. Meier, T. Reisinger, and W. Gebhardt, *J. Appl. Phys.* **80**, 4049 (1996).